

# Accepted Manuscript

A detailed pathway analysis of the chemical reaction system  
generating the Martian vertical ozone profile

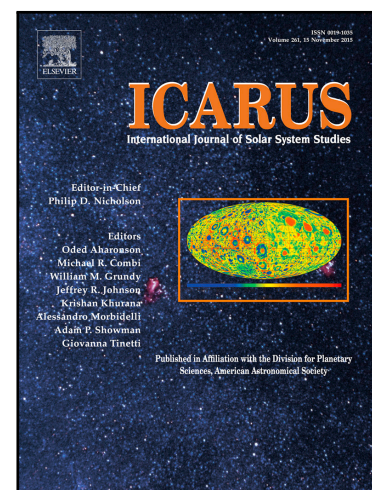
Joachim W. Stock, Christopher S. Blaszczyk-Boxe, Ralph Lehmann,  
J.Lee Grenfell, A.Beate C. Patzer, Heike Rauer, Yuk L. Yung

PII: S0019-1035(16)30818-1  
DOI: [10.1016/j.icarus.2016.12.012](https://doi.org/10.1016/j.icarus.2016.12.012)  
Reference: YICAR 12300

To appear in: *Icarus*

Received date: 7 December 2015  
Revised date: 15 November 2016  
Accepted date: 5 December 2016

Please cite this article as: Joachim W. Stock, Christopher S. Blaszczyk-Boxe, Ralph Lehmann, J.Lee Grenfell, A.Beate C. Patzer, Heike Rauer, Yuk L. Yung, A detailed pathway analysis of the chemical reaction system generating the Martian vertical ozone profile, *Icarus* (2016), doi: [10.1016/j.icarus.2016.12.012](https://doi.org/10.1016/j.icarus.2016.12.012)



This is a PDF file of an unedited manuscript that has been accepted for publication. As a service to our customers we are providing this early version of the manuscript. The manuscript will undergo copyediting, typesetting, and review of the resulting proof before it is published in its final form. Please note that during the production process errors may be discovered which could affect the content, and all legal disclaimers that apply to the journal pertain.

## Highlights

- Determination of all significant  $O_3$  producing and consuming pathways and quantification of their contributions in the Martian atmosphere with help of an automated computer algorithm.
- $O_3$  production results from  $CO_2$  and  $O_2$  photolysis.
- $O_3$  is consumed by catalytic cycles involving  $HO_x$  ( $=H+OH+HO_2$ ).
- The Martian atmosphere can be divided into two chemically distinct regions according to the  $O(^3P):O_3$  ratio.
- Vertical transport of  $O(^3P)$  from upper layers downwards into the  $O_3$  layer at around 50 km altitude provides an additional source of  $O_x$  ( $=O+O_3$ ), which is pivotal to the formation of the Martian  $O_3$  volume mixing ratio maximum.

# A detailed pathway analysis of the chemical reaction system generating the Martian vertical ozone profile

Joachim W. Stock<sup>a,b,\*</sup>, Christopher S. Blaszczyk-Boxe<sup>c,d</sup>, Ralph Lehmann<sup>e</sup>, J. Lee Grenfell<sup>b,f</sup>, A. Beate C. Patzer<sup>f</sup>, Heike Rauer<sup>b,f</sup>, Yuk L. Yung<sup>g</sup>

<sup>a</sup>Instituto de Astrofísica de Andalucía - CSIC, Glorieta de la Astronomía s/n, 18008 Granada, Spain

<sup>b</sup>Institut für Planetenforschung, Deutsches Zentrum für Luft und Raumfahrt (DLR), Rutherfordstr. 2, 12489 Berlin, Germany

<sup>c</sup>Department of Chemistry and Environmental Science, Medgar Evers College-City University of New York, 1650 Bedford Avenue, Brooklyn, NY 11235, United States

<sup>d</sup>CUNY's Graduate Center's Earth and Environmental Sciences Department and Chemistry Divisions, New York, NY 10016, United States

<sup>e</sup>Alfred-Wegener-Institut, Helmholtz-Zentrum für Polar- und Meeresforschung (AWI), Telegrafenberg A43, 14473 Potsdam, Germany

<sup>f</sup>Zentrum für Astronomie und Astrophysik (ZAA), Technische Universität Berlin (TUB), Hardenbergstr. 36, 10623 Berlin, Germany

<sup>g</sup>Division of Geological and Planetary Sciences, California Institute of Technology, 1200 East California Boulevard, Pasadena, CA 91125, United States

## Abstract

Atmospheric chemical composition is crucial in determining a planet's atmospheric structure, stability, and evolution. Attaining a quantitative understanding of the essential chemical mechanisms governing atmospheric composition is nontrivial due to complex interactions between chemical species. Trace species, for example, can participate in catalytic cycles – affecting the abundance of major and other trace gas species. Specifically, for Mars, such cycles dictate the abundance of its primary atmospheric constituent, carbon dioxide (CO<sub>2</sub>), but also for one of its trace gases, ozone (O<sub>3</sub>). The identification of chemical pathways/cycles by hand is extremely demanding; hence, the application of numerical methods, such as the *Pathway Analysis Program* (PAP), is crucial to analyze and quantitatively exemplify chemical reaction networks. Here, we carry out the first automated quantitative chemical pathway analysis of Mars' atmosphere with respect to O<sub>3</sub>. PAP was applied to JPL/Caltech's 1-D updated photochemical Mars model's output data. We determine all significant chemical pathways and their contribution to O<sub>3</sub> production and consumption (up to 80 km) in order to investigate the mechanisms causing the characteristic shape of the O<sub>3</sub> volume mixing ratio profile, i.e. a ground layer maximum and an ozone layer at ~ 50 km. These pathways explain why an O<sub>3</sub> layer is present, why it is located at that particular altitude and what the different processes forming the near-surface and middle atmosphere O<sub>3</sub> maxima are. Furthermore, we show that the Martian atmosphere can be divided into two chemically distinct regions according to the O(<sup>3</sup>P):O<sub>3</sub> ratio. In the lower region (below approximately 24 km altitude) O<sub>3</sub> is the most abundant O<sub>x</sub> (= O<sub>3</sub> + O(<sup>3</sup>P)) species. In the upper region (above approximately 24 km altitude), where the O<sub>3</sub> layer is located, O(<sup>3</sup>P) is the most abundant O<sub>x</sub> species. Earlier results concerning the formation of O<sub>3</sub> on Mars can now be explained with the help of chemical pathways leading to a better understanding of the vertical O<sub>3</sub> profile.

**Keywords:** Atmospheres, chemistry, Atmospheres, composition, Mars, Mars, atmosphere, Photochemistry,

## 1. Introduction

Ozone (O<sub>3</sub>) is one of the most important chemical species for understanding the chemistry in the carbon dioxide (CO<sub>2</sub>) dominated atmosphere of Mars. In the early 1970's McElroy and Donahue (1972) and Parkinson and Hunten (1972) demonstrated that the chemistry, which stabilizes CO<sub>2</sub>, is dominated by catalytic cycles involving odd hydrogen (HO<sub>x</sub> = H + OH + HO<sub>2</sub>) species, formed by water vapor (H<sub>2</sub>O) photolysis (see also e.g. Atreya and Gu, 1994; Nair et al., 1994; Yung and DeMore, 1999; Stock et al., 2012a,b). Observations and theoretical models of O<sub>3</sub> and H<sub>2</sub>O in the Martian atmosphere have clearly shown an anticorrelation between these two molecules (e.g. Lane et al., 1973; Clancy et al., 1996; Lefèvre et al., 2004;

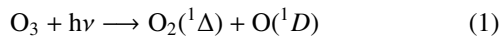
Montmessin et al., 2004; Smith, 2004; Fast et al., 2006a; Perrier et al., 2006), suggesting that O<sub>3</sub> is a good indicator for extremely low OH and HO<sub>2</sub> volume mixing ratios and therefore “dry” conditions. Furthermore, O<sub>3</sub> can act in CO<sub>2</sub> forming pathways as a source of atomic oxygen or as a catalyst (Yung and DeMore, 1999; Stock et al., 2012a).

On Mars, atmospheric O<sub>3</sub> was first detected in the southern polar region by ultraviolet (UV) spectrometers aboard Mariner 7 during its flyby in 1969 (Barth and Hord, 1971). Closer investigations of the Hartley O<sub>3</sub> absorption feature at 255 nm wavelength by the Mariner 9 UV spectrometer revealed not only latitudinal and seasonal variations in O<sub>3</sub> concentrations (Barth et al., 1973) but also indicated the above-mentioned anticorrelation between O<sub>3</sub> and H<sub>2</sub>O in the atmosphere of Mars (Lane et al., 1973). Noxon et al. (1976) first observed the 1.27 μm O<sub>2</sub>(<sup>1</sup>Δ) dayglow emission line in the Martian atmo-

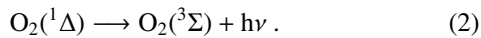
\*Corresponding author

Email address: joachimstock14@gmail.com (Joachim W. Stock)

sphere, which results from  $O_3$  photodissociation



emission of a photon



Traub et al. (1979) applied this detection method to study and compare  $O_3$  concentrations in the equatorial region between  $\pm 20^\circ$  latitude and the polar regions beyond  $\pm 45^\circ$  latitude. In the following, the  $1.27 \mu m$   $O_2(^1\Delta)$  dayglow emission has been used to map  $O_3$  and to investigate its seasonal and latitudinal behavior (e.g. Krasnopolsky and Bjoraker, 2000; Novak et al., 2002; Krasnopolsky, 2003). A ground based observational method to measure  $O_3$  directly was introduced by Espenak et al. (1991) using infrared (IR) heterodyne spectroscopy, which provided a higher spatial resolution than  $O_2(^1\Delta)$  dayglow observations. IR heterodyne spectra near the  $9.7 \mu m$  absorption band have been taken with the NASA/Goddard Space Flight Center IRHS (Infrared Heterodyne Spectrometer) and HIPWAC (Heterodyne Instrument for Planetary Wind And Composition) and analysed by Fast et al. (2006a,b), indicating that the vertical distribution of  $O_3$  plays an important role to understand the deviations from the strict anticorrelation between  $O_3$  and  $H_2O$  column integrated abundances (see also Lefèvre et al., 2004).

The early Mars “wet” model of Parkinson and Hunten (1972) already predicted an  $O_3$  concentration layer at an atmospheric height around  $z \approx 32$  km. This layer was finally discovered at approximately  $z \approx 40$  km altitude by Krasnopolsky et al. (1975) (see also Krasnopolsky and Parshev, 1979), using measurements obtained by the Mars 5 orbiter at the daytime limb and evening terminator. Later solar occultation observations close to the evening terminator near the northern spring equinox by an UV spectrometer aboard the Phobos 2 spacecraft confirmed the existence of the  $O_3$  concentration maximum between  $z = 42$  km to  $z = 45$  km in the equatorial region (Blamont and Chassefière, 1993).

ESA’s Mars Express (MEX) mission led to a significant leap in the exploration of Mars’  $O_3$ . Using the UV spectrometer of the SPICAM (SPectroscopy for the Investigation of the Characteristics of the Atmosphere of Mars) instrument (Bertaux et al., 2000, 2006), Lebonnois et al. (2006) and Perrier et al. (2006) measured the vertical and global distribution of  $O_3$ , accumulating data from more than one year of observations. This work was supplemented by three dimensional modeling efforts by Lefèvre et al. (2004), who investigated the seasonal, latitudinal and diurnal behavior of  $O_3$  by employing the LMD (Laboratoire de Météorologie Dynamique) GCM (General Circulation Model). Lefèvre et al. (2008) pointed out the potential significance of the heterogeneous chemistry upon ice cloud particles, which act as an effective  $HO_x$  sink (resulting in “dryer” conditions), bringing better coincidence between SPICAM  $O_3$  and ground based  $O_3$  and  $H_2O_2$  observations as well as model results. Later observations with the MARCI (MARs Color Imager) instrument onboard MRO (Mars Reconnaissance Orbiter), however, did not provide strong evidence of a correlation between  $O_3$  and clouds (Clancy et al., 2016).

Here, we investigate

- (a) why an  $O_3$  layer is present,
- (b) why it is located at that particular altitude and
- (c) what the different processes forming the near-surface and middle atmosphere ozone maxima are,

by studying how  $O_3$  is produced and consumed on Mars. The problem of explaining direct  $O_3$  production and consumption can be addressed by inspecting calculated reaction rates and searching for the one with the largest rate. However, these reactions can be involved in both fast  $O_3$  null cycles (no net  $O_3$  production or consumption) and catalytic  $O_3$  production or loss pathways. The latter pathways are relevant for explaining the  $O_3$  volume mixing ratio profile. The role of catalytic cycles for  $O_3$  formation and consumption in Earth’s atmosphere has been demonstrated by e.g. Bates and Nicolet (1950) and Crutzen (1970). Note, that the presence of catalytic species on Mars has a dramatic impact on the chemical composition of the atmosphere (McElroy and Donahue, 1972; Parkinson and Hunten, 1972), hence it is expected, that catalytic cycles are also relevant to the  $O_3$  formation and consumption on Mars.

Generally, it is very difficult to find a complete set of relevant production and consumption pathways of a given species. Therefore, we use the *Pathway Analysis Program* (PAP, Lehmann, 2004), which enables the determination of all dominant pathways in reaction networks. The algorithm has been successfully applied to very different topics such as Earth’s stratospheric  $O_3$  (Lehmann, 2004; Grenfell et al., 2006), Earth’s mesosphere and ionosphere (Verronen et al., 2011; Verronen and Lehmann, 2013, 2015), the Martian  $CO_2$  stability problem (Stock et al., 2012a,b), and biomarker chemistry on Earth-like extrasolar planets orbiting M-dwarf stars (Grenfell et al., 2013).

Here, we are particularly interested in the shape of the vertical  $O_3$  profile under mean atmospheric conditions and the chemical cycles which determine the location of the  $O_3$  layer. Therefore, we apply for the first time the computer algorithm PAP to the output of the updated version of the JPL/Caltech KINETICS model of the Martian atmosphere (Nair et al., 1994; Boxe et al., 2014) to identify all significant chemical pathways and quantify their contribution to  $O_3$  formation and consumption up to 80 km altitude.

## 2. Method

### 2.1. Martian atmospheric photochemical column model

To study the  $O_3$  profile in the Martian atmosphere under global average conditions with the help of the *Pathway Analysis Program* (PAP, Lehmann, 2004), the output of the updated version of the JPL/Caltech Martian atmospheric photochemical column model has been employed, which was described in detail by Nair et al. (1994). The version of the photochemical kinetics model used here provides the mathematical solution of a system of coupled one-dimensional continuity equations

$$\frac{\partial}{\partial t} n_i(z, t) + \frac{\partial}{\partial z} \Phi_i(z, t) = \mathcal{P}_i(n_1, \dots, n_{N_S}) - \mathcal{L}_i(n_1, \dots, n_{N_S}) \quad (3)$$

for  $N_S = 29$  species ( $O(^3P)$ ,  $O(^1D)$ ,  $O_2(^3\Sigma)$ ,  $O_2(^1\Delta)$ ,  $O_3$ ,  $N(^4S)$ ,  $N(^2D)$ ,  $N_2$ ,  $N_2O$ ,  $NO$ ,  $NO_2$ ,  $NO_3$ ,  $N_2O_5$ ,  $HNO_2$ ,  $HNO_3$ ,  $HO_2NO_2$ ,  $H$ ,  $H_2$ ,  $H_2O$ ,  $OH$ ,  $HO_2$ ,  $H_2O_2$ ,  $CO$ ,  $CO_2$ ,  $HCO_2$ ,  $O^+$ ,  $O_2^+$ ,  $CO_2^+$ ,  $CO_2H^+$ ), where  $z$  denotes the atmospheric altitude,  $\mathcal{P}_i(n_1, \dots, n_{N_S})$  the production rate and  $\mathcal{L}_i(n_1, \dots, n_{N_S})$  the loss rate of species  $S_i$  with the related number density  $n_i$ . The vertical flux of species  $S_i$  is calculated via

$$\Phi_i = -D_i \left( \frac{dn_i}{dz} + \frac{n_i}{H_i} + \frac{n_i(1 + \alpha_i)}{T} \frac{dT}{dz} \right) - K \left( \frac{dn_i}{dz} + \frac{n_i}{H} + \frac{n_i}{T} \frac{dT}{dz} \right), \quad (4)$$

where  $D_i$ ,  $H_i$  and  $\alpha_i$  are the molecular diffusion coefficient, the scale height and the thermal diffusion factor of species  $S_i$ , respectively.  $K$ ,  $H$ , and  $T$  denote the eddy diffusion coefficient, the scale height of the background atmosphere and the local gas temperature, respectively. The vertical grid covers the atmosphere from the Martian surface up to 240 km in 2 km intervals. For the chemical pathway analysis, we used the steady state solution of the photochemical model for fixed temperature and pressure profiles (for details see Nair et al., 1994). The chemical reaction system includes 149 reactions (for details see Stock et al., 2012a; Boxe et al., 2014). In contrast to Stock et al. (2012a), we distinguish between the excited state  $O_2(^1\Delta)$  and the ground state  $O_2(^3\Sigma)$  of molecular oxygen. Additionally, the  $HCO_2$  chemistry introduced by Boxe et al. (2014) is included in the chemical model. Reaction rate coefficients are updated according to Sander et al. (2011).

Since the  $O_3$  volume mixing ratio exhibits latitudinal, diurnal and seasonal variations, the utilization of one-dimensional models is limited. For example, horizontal transport cannot be described, i.e. the effect of atmospheric circulation is parameterized within the eddy diffusion profile, which is derived from aerosol measurements (see Nair et al., 1994, and references therein). Nevertheless, in order to discuss the  $O_3$  chemistry under global mean conditions, it is useful to abstain from the three-dimensional treatment in favor of a more detailed description of the chemical reaction network. This approach is strengthened by the fact, that the results of the  $O_3$  volume mixing ratio profile calculated with the help of the JPL/Caltech photochemical model are within observational constraints (Nair et al., 1994).

For the description of the photolysis rate constants a diurnally averaged solar radiation field for ca.  $30^\circ$  latitude at equinox is assumed. The diurnally averaged radiation corresponds to the radiation at 7:15 a.m. LTST (local true solar time) and 4:45 p.m. LTST. It is well known that the  $O_3$  concentration in the  $O_3$  layer considerably varies diurnally since the chemical lifetime of  $O_3$  is shorter than one day (see e.g. Nair et al., 1994; Lefèvre et al., 2004; Perrier et al., 2006). Note, that although we assume a diurnally averaged radiation field, the resulting  $O_3$  concentration does not necessarily represent the diurnally averaged  $O_3$  concentration.

The eddy diffusion profile is given by Nair et al. (1994), their Fig. 1(b). The eddy diffusion coefficient ( $K$ ) is  $10^5 \text{ cm}^2 \text{ s}^{-1}$  at the surface and increases exponentially up to  $10^7 \text{ cm}^2 \text{ s}^{-1}$  at

$z = 40 \text{ km}$  consistent with aerosol measurements (Toon et al., 1977; Anderson and Leovy, 1978; Chassefière et al., 1992; Korabely et al., 1993). Between  $z = 40 \text{ km}$  and  $z = 70 \text{ km}$ ,  $K$  is constant. The value is chosen to reproduce the  $O_2$  volume mixing ratio as discussed by Nair et al. (1994). Rosenqvist and Chassefière (1995) reexamined the relationship between eddy mixing and  $O_2$  concentration, which is consistent with the value of the eddy diffusion coefficient used here. Between  $z = 70 \text{ km}$  and  $z = 100 \text{ km}$ , the eddy diffusion coefficient increases again exponentially with increasing altitude up to  $K = 10^8 \text{ cm}^2 \text{ s}^{-1}$  to match the abundance of atomic oxygen at the thermosphere.

Water vapor ( $H_2O$ ) is the most important reservoir species for  $HO_x$  radicals. Its abundance on Mars is mainly controlled by condensation/evaporation and the global circulation and consequently exhibits diurnal, seasonal and latitudinal variations (see for example Barker, 1976; Jakosky and Farmer, 1982; Jakosky, 1985; Houben et al., 1997; Richardson and Wilson, 2002; Montmessin et al., 2004). However, one-dimensional models generally use fixed water profiles. Here we utilize the standard  $H_2O$  profile employed by Nair et al. (1994) in order to represent mean conditions, i.e. we assume a well mixed water abundance in the lower atmosphere up to the hygropause, the height where  $H_2O$  becomes saturated. Above  $z \approx 60 \text{ km}$ , where the  $H_2O$  saturation profile has a minimum,  $H_2O$  is undersaturated and its abundance is determined by photochemistry.

## 2.2. Pathway Analysis Program

The *Pathway Analysis Program* (PAP) allows for the identification of chemical pathways in arbitrarily given reaction networks. Additionally, it quantifies the efficiency of the pathways by computing the corresponding rates. In this way, the relative importance of the different, competing chemical pathways can be determined. PAP was described in more detail by Lehmann (2004) and some applications with respect to the  $CO_2$  formation on Mars were discussed by Stock et al. (2012a,b).

In accordance with Stock et al. (2012a) we denote the rate of the net change of species  $S_i$  caused by pathway  $P_k$  by

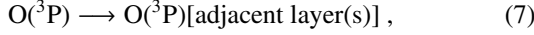
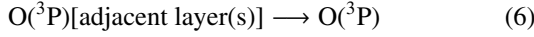
$$\varphi_{ik} = |m_{ik}| f_k, \quad i = 1, \dots, N_S, \quad k = 1, \dots, N_P, \quad (5)$$

where  $m_{ik}$  is the stoichiometric coefficient of species  $S_i$  in the net reaction of pathway  $P_k$  with its rate  $f_k$ .  $N_P$  is the total number of pathways.

In order to identify the chemical pathways in the Martian atmosphere and to quantify their efficiencies, we apply the PAP algorithm to the steady-state solution of the JPL/Caltech KINETICS model for each atmospheric layer separately (see Stock et al., 2012a, for further details).

In general, chemical production  $\mathcal{P}_i$  and chemical consumption  $\mathcal{L}_i$  in planetary atmospheres can differ even under steady state conditions if other sources or sinks apart from chemical reactions are present – such as for instance vertical diffusion (see Eq. (3)). The analysis method can be extended to account for such processes by introducing pseudo reactions describing emission, transport processes etc. Since  $O(^3P)$  is strongly af-

ected by vertical transport, we include two pseudo reactions:



representing the transport into or out of a layer centered at altitude  $z$ .

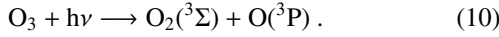
We calculate the associated reaction rates under steady state conditions (i.e.  $\partial n_{\text{O}(^3\text{P})}/\partial t = 0$ ) by using Eq. (3) and treating the term  $\partial \Phi_{\text{O}(^3\text{P})}/\partial z$  according to its sign as a *pseudo production rate*

$$r_{\text{O}(^3\text{P})}^{\text{gain}} = \begin{cases} -\partial \Phi_{\text{O}(^3\text{P})}/\partial z & , \partial \Phi_{\text{O}(^3\text{P})}/\partial z < 0 \\ 0 & , \text{otherwise} \end{cases} \quad (8)$$

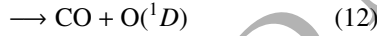
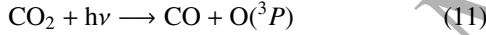
or a *pseudo consumption rate*

$$r_{\text{O}(^3\text{P})}^{\text{loss}} = \begin{cases} \partial \Phi_{\text{O}(^3\text{P})}/\partial z & , \partial \Phi_{\text{O}(^3\text{P})}/\partial z > 0 \\ 0 & , \text{otherwise} \end{cases} \quad (9)$$

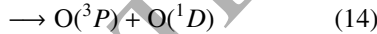
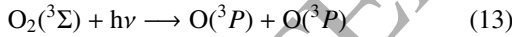
There are several  $\text{O}_3$  photolysis channels leading to ground state atomic oxygen  $\text{O}(^3\text{P})$ , electronically excited state of atomic oxygen ( $\text{O}(^1\text{D})$ ), ground state molecular oxygen  $\text{O}_2(^3\Sigma)$  and/or electronically excited molecular oxygen ( $\text{O}_2(^1\Delta)$ ) (see Matsumi et al., 2002, for example). The most important ones in the Martian atmosphere are the spin-allowed channels (1) and



Another considerable source of  $\text{O}(^3\text{P})$  and  $\text{O}(^1\text{D})$  are the photolysis of  $\text{CO}_2$



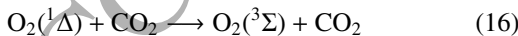
and of  $\text{O}_2(^3\Sigma)$



with different reaction channels. The collisional deactivation of  $\text{O}(^1\text{D})$



and of  $\text{O}_2(^1\Delta)$

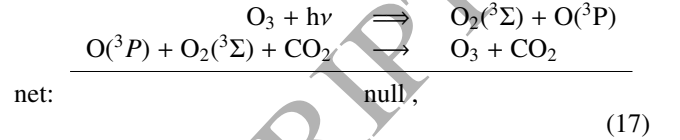


with the most abundant species in the Martian atmosphere are relatively fast, especially in the lower atmospheric parts. As a result, the combinations  $\{(1), (15), (16)\}$ ,  $\{(12), (15)\}$  and  $\{(14), (15)\}$  may occur within the pathways found by the *PAP* algorithm. As  $\{(1)\}$  has the same net effect as reaction (10), for each pathway  $P$  containing the reactions (1), (15) and (16), there exists a competing pathway  $P'$  containing the set of reactions as  $P$ , but with reaction (10) instead of the reactions (1), (15) and (16). Analogously, for each pathway  $P$  containing the reactions (12) and (15) there is a competing pathway  $P'$  containing the set of reactions as  $P$ , but with reaction (11) instead of the reactions (12) and (15). Since the different photolysis channels are not relevant for the analysis, we simplify

the representation of the pathways containing different photolysis channels by merging the pathways  $P$  and  $P'$  into pathway families. In other words, we distinguish between electronically excited and ground state atoms/molecules, when running the JPL/Caltech KINETICS model and the *PAP*, but introduce a simplified notation, using the “ $\Rightarrow$ ”-symbol, if several reaction channels with and without subsequent quenching are relevant, when discussing the results of the *PAP*.

### 2.3. Additional definitions

Ozone can be recycled by null pathways, for instance



which do not change directly the  $\text{O}_3$  concentration. Hence, for explaining the  $\text{O}_3$  concentration, it is useful to eliminate their effect from the production and consumption rates of  $\text{O}_3$ . Therefore, we distinguish the rate of null pathways

$$\hat{N}_i = \sum_{\{k|m_{ik}=0\}}^{N_P} \tilde{m}_{ik} f_k \quad (18)$$

recycling  $S_i=\text{O}_3$   $\tilde{m}_{ik} \in \mathbb{N}$  times in pathway  $P_k$  from the rate of production

$$\hat{P}_i = \sum_{\{k|m_{ik}>0\}}^{N_P} m_{ik} f_k \quad (19)$$

by chemical pathways forming  $S_i=\text{O}_3$  from long-lived oxygen reservoir species like  $\text{CO}_2$  and  $\text{O}_2$  and from the rate of consumption

$$\hat{L}_i = \sum_{\{k|m_{ik}<0\}}^{N_P} |m_{ik}| f_k \quad (20)$$

by chemical pathways converting  $S_i=\text{O}_3$  to long-lived oxygen reservoir species. Since the rate of each reaction is completely distributed to the pathways  $P_k$ , including null pathways, it follows directly that

$$\mathcal{P}_i = \hat{P}_i + \hat{N}_i \quad (21)$$

$$\mathcal{L}_i = \hat{L}_i + \hat{N}_i. \quad (22)$$

To ease the discussion of our results, we define the production rate by reactions and by chemical pathways in volume mixing ratio

$$\mathcal{P}_i(z) := \frac{\mathcal{P}_i(z)}{n_{\text{tot}}(z)} \quad (23)$$

$$\mathcal{L}_i(z) := \frac{\mathcal{L}_i(z)}{n_{\text{tot}}(z)}, \quad (24)$$

where

$$n_{\text{tot}}(z) = \sum_{i=1}^{N_S} n_i(z) \quad (25)$$

is the altitude dependent total number density.

Since steady state conditions ( $\partial n_i(z, t)/\partial t = 0$ ) are assumed and the change in volume mixing ratio of  $S_i=O_3$  by vertical transport is relatively small in comparison to the change in volume mixing ratio by chemical production or loss (about  $\lesssim 1\%$  in the altitude regions which contain the  $O_3$  maxima), the term  $\partial \Phi_i(z, t)/\partial z$  in Eq. (3) can be neglected and it follows

$$\mathcal{P}_i(z) = \mathcal{L}_i(z). \quad (26)$$

Using Eq. (21), Eq. (22) and Eq. (26) we find

$$\hat{\mathcal{P}}_i(z) = \hat{\mathcal{L}}_i(z). \quad (27)$$

As a measure of how fast a species  $S_i$  undergoes chemical loss reactions, it is useful to define the pseudo first order loss rate coefficient<sup>1</sup>

$$\Lambda_i(z) := \frac{\mathcal{L}_i(z)}{n_i(z)}. \quad (28)$$

Thus the steady state volume mixing profiles can be expressed by

$$\frac{n_i(z)}{n_{\text{tot}}(z)} = \frac{\mathcal{P}_i(z)}{\Lambda_i(z)}, \quad (29)$$

using Eq. (23), Eq. (26) and Eq. (28). Although Eq. (29) is formally correct, the right hand side depends on  $S_i=O_3$ , since  $\mathcal{P}_i(z)$  and  $\Lambda_i(z)$  contain the rate of null pathways (see Eq. (21), (22), (23) and (28)). This means both sides of Eq (29) depend on  $S_i=O_3$  and hence this equation is not helpful for explaining the mechanisms generating the  $O_3$  volume mixing ratio profile. Therefore, in analogy to Eq. (28) we define

$$\hat{\Lambda}_i(z) := \frac{\hat{\mathcal{L}}_i(z)}{n_i(z)} \quad (30)$$

Thus the steady state volume mixing profiles can also be expressed by

$$\frac{n_i(z)}{n_{\text{tot}}(z)} = \frac{\hat{\mathcal{P}}_i(z)}{\hat{\Lambda}_i(z)} \quad (31)$$

using Eq. (24), Eq. (30) and Eq. (27).

### 3. Results and discussion

#### 3.1. The $O_3$ volume mixing ratio profile

Figure 1(a) shows among others the vertical profile of  $O_3$  as calculated by the updated version of the Caltech/JPL KINETICS model for the Martian atmosphere. The  $O_3$  volume mixing ratio profile exhibits two maxima: one near the Martian surface, henceforth called *ground layer  $O_3$  maximum*, and another one at an atmospheric height around  $z = 50$  km altitude (corresponding to a concentration maximum at  $z \approx 44$  km), henceforth  *$O_3$  layer*. Figure 1(a) also shows the volume mixing ratio of  $O(^3P)$ , which increases monotonically with increasing altitude. The profiles of  $O(^3P)$  and  $O_3$  intersect at about  $z \approx 24$  km. Consequently, we find two distinct chemical regions: The lower region ( $n_{O(^3P)} < n_{O_3}$ ) contains the ground layer  $O_3$  maximum.

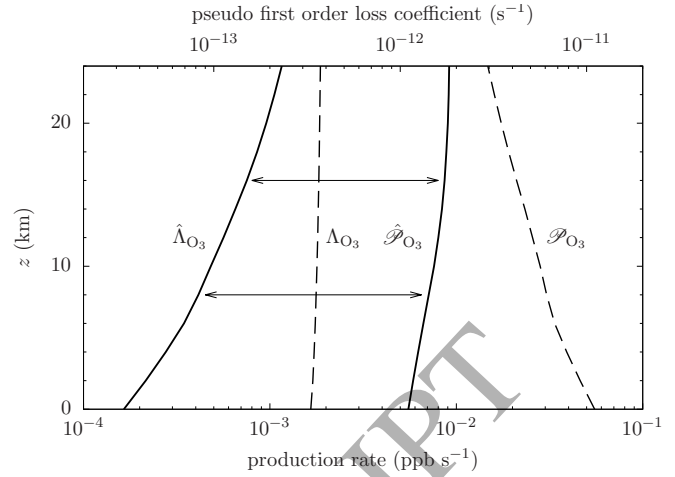


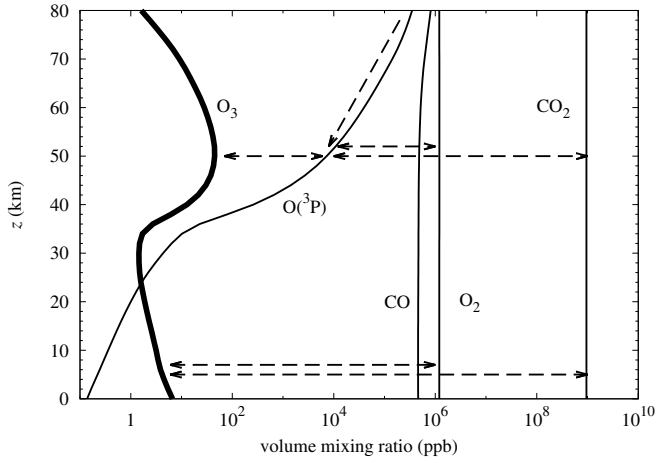
Figure 2: Pseudo first order  $O_3$  loss rate coefficients  $\Lambda_{O_3}$  and  $\hat{\Lambda}_{O_3}$  (left hand side, upper axis) and  $O_3$  production rates  $\mathcal{P}_{O_3}$  and  $\hat{\mathcal{P}}_{O_3}$  (right hand side, lower axis) in the lower region. Solid lines refer to the production rate  $\hat{\mathcal{P}}_{O_3}$  and pseudo first order loss rate coefficient  $\hat{\Lambda}_{O_3}$  via pathways according to Eq. (24) and Eq. (30). Dashed lines refer to the production rate  $\mathcal{P}_{O_3}$  and pseudo first order loss rate coefficient  $\Lambda_{O_3}$  via reactions. Since the x-axis is in logarithmic scale, the difference between the solid lines, indicated by the length of the horizontal arrows, describes the ratio  $\mathcal{P}_{O_3} : \hat{\Lambda}_{O_3}$ , which is the volume mixing ratio of  $O_3$  according to Eq. (31).

Here, the  $O_3$  abundance is directly controlled by the reservoir species  $CO_2$  and  $O_2$  (indicated by the lower two arrows in Fig. 1(a)). The upper region ( $n_{O(^3P)} > n_{O_3}$ ) includes the  $O_3$  layer. Here, the  $O_3$  concentration is controlled by  $O(^3P)$ , which in turn is regulated by  $CO_2$  and  $O_2$  (indicated by the upper two horizontal arrows in Fig. 1(a)) and transport (indicated by the diagonal arrow in Fig. 1(a)). Both regions are chemically quite different (see below) and will be analyzed separately.

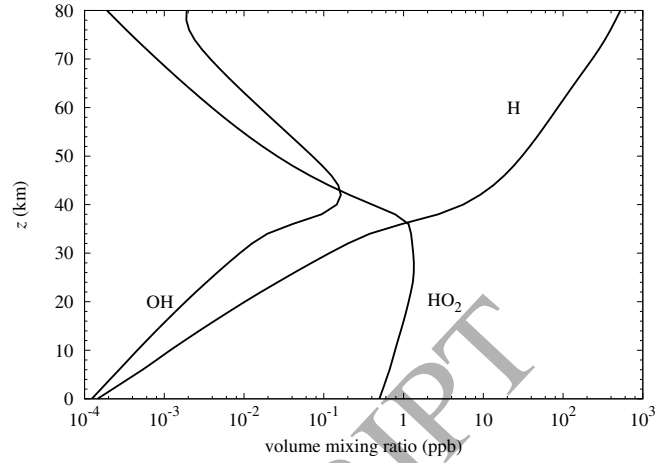
#### 3.2. Chemical $O_3$ pathways in the lower region

To understand the shape of the  $O_3$  profile in the lower region, Fig. 2 shows production rates  $\mathcal{P}_{O_3}(z)$  and  $\hat{\mathcal{P}}_{O_3}(z)$ , as well as the first order pseudo loss rate coefficients  $\Lambda_{O_3}(z)$  and  $\hat{\Lambda}_{O_3}(z)$ . Due to the significant amount of  $O_3$  recycled via pathway (17) in the lower region it follows that  $\mathcal{P}_{O_3}(z) \gg \hat{\mathcal{P}}_{O_3}(z)$  and  $\Lambda_{O_3}(z) \gg \hat{\Lambda}_{O_3}(z)$  (see Section 2.3). In the logarithmic plot (Fig. 2), the lengths of the arrows correspond to the  $O_3$  volume mixing ratio (see also Eq. (31)). In the lower region,  $\hat{\mathcal{P}}_{O_3}(z)$  decreases about a factor of two with decreasing altitude, while  $\hat{\Lambda}_{O_3}(z)$  decreases about a factor of seven with decreasing altitude, indicating that the ground layer  $O_3$  maximum is caused by the decrease of the  $\hat{\Lambda}_{O_3}$  with decreasing altitude (see Eq. (31)). The relative contributions of all pathways consuming/forming  $O_3$  in the lower region are shown in detail in Fig. 3 and will be discussed in the following sections.

<sup>1</sup>Sometimes called the implicit loss coefficient (see e.g. Jacobson, 2005).



(a) Odd oxygen ( $O(^3P)$ ,  $O_3$ ), molecular oxygen ( $O_2$ ), carbon monoxide (CO), carbon dioxide ( $CO_2$ )



(b) Odd hydrogen species (H, OH,  $HO_2$ ).

Figure 1: Volume mixing ratios of selected atomic and molecular species in the Martian atmosphere calculated by the Caltech/JPL KINETICS model. Dashed arrows in the left hand panel indicate the exchange of oxygen atoms between species. There are one long-lived source of  $O_3$  above  $z \approx 24$  km, namely  $O(^3P)$  and two long-lived sources of  $O_3$  below  $z \approx 24$  km, namely  $O_2$  and  $CO_2$ . The processes are explained in more detail in Section 3.2 and Section 3.3.

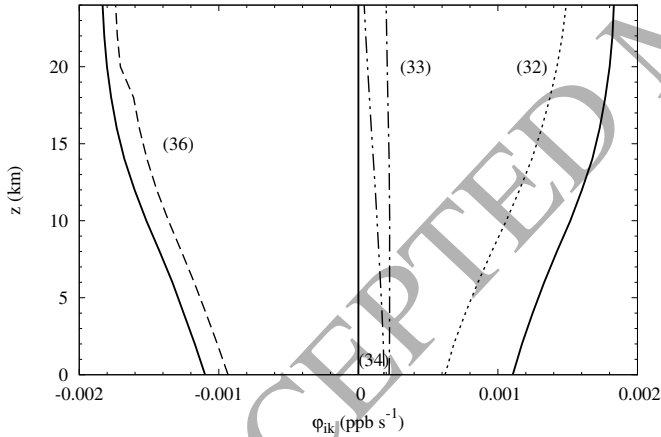


Figure 3: Rates  $\phi_{ik}$  of  $O_3$  production/consumption pathways in the lower region. Loss rates are indicated with a negative sign. The solid line on the right hand side indicates the production of  $O_3$  by all  $O_3$  formation pathways. The solid line on the left hand side indicates the consumption of  $O_3$  by all  $O_3$  consumption pathways. Bracketed numbers refer to pathways given in the text and Tab. 1.

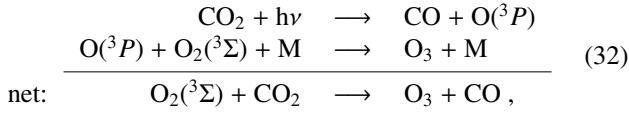
Table 1: Percentage contribution of the dominant  $O_3$  production and consumption pathways at the  $O_3$  ground layer maximum.

| production  |  |  |            |
|-------------|--|--|------------|
| (32)        | $CO_2 + h\nu \longrightarrow CO + O(^3P)$<br>$O(^3P) + O_2(^3\Sigma) + M \longrightarrow O_3 + M$  |  |            |
| net:        | $O_2(^3\Sigma) + CO_2 \longrightarrow O_3 + CO$  |  | <b>56%</b> |
| (33)        | $O_2(^3\Sigma) + h\nu \longrightarrow O(^3P) + O(^3P)$<br>$2 \cdot (O(^3P) + O_2(^3\Sigma) + M \longrightarrow O_3 + M)$   |  |            |
| net:        | $3 \cdot O_2(^3\Sigma) \longrightarrow 2 \cdot O_3$  |  | <b>20%</b> |
| (34)        | $OH + CO \longrightarrow CO_2 + H$<br>$H + O_2(^3\Sigma) + M \longrightarrow HO_2 + M$<br>$HO_2 + NO \longrightarrow NO_2 + OH$<br>$NO_2 + h\nu \longrightarrow NO + O(^3P)$<br>$O(^3P) + O_2(^3\Sigma) + M \longrightarrow O_3 + M$ |  |            |
| net:        | $2 \cdot O_2(^3\Sigma) + CO \longrightarrow O_3 + CO_2$  |  | <b>17%</b> |
| consumption |  |  |            |
| (36)        | $O_3 + h\nu \Longrightarrow O_2(^3\Sigma) + O(^3P)$<br>$O(^3P) + HO_2 \longrightarrow OH + O_2(^3\Sigma)$<br>$OH + CO \longrightarrow CO_2 + H$<br>$H + O_2(^3\Sigma) + M \longrightarrow HO_2 + M$                                  |  |            |
| net:        | $O_3 + CO \longrightarrow O_2(^3\Sigma) + CO_2$  |  | <b>85%</b> |

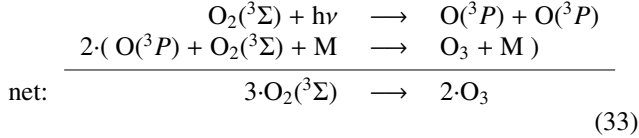


### 3.2.1. Ozone production (lower region)

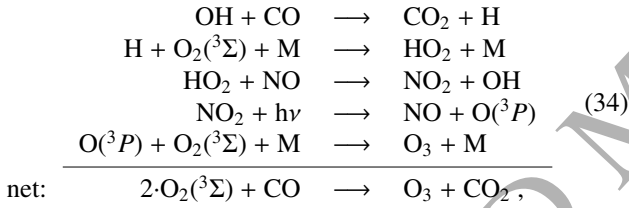
Figure 3 and Tab. 1 show that the majority of  $O_3$  in the lower region is formed via a Chapman-like  $O_3$  production pathway



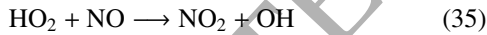
i.e.  $O(^3P)$ , which reacts with  $O_2(^3\Sigma)$  to produce  $O_3$ , is formed by  $\text{CO}_2$  photolysis and M is  $\text{CO}_2$ . The original Chapman  $O_3$  production pathway



– well known for operating in Earth's atmosphere (M is  $\text{N}_2$  or  $\text{O}_2$ ) yielding the notable  $O_3$  layer – is also active on Mars with  $\text{M}=\text{CO}_2$ . However, on Mars, pathway (33) is less efficient than pathway (32), because of the large  $\text{CO}_2:\text{O}_2$  ratio in the Martian atmosphere. The  $O_3$  production decreases with decreasing altitude, because of the decreasing rates of the  $\text{CO}_2$  and  $\text{O}_2$  photolysis reactions with decreasing altitude. Furthermore, we identify another significant  $O_3$  production pathway



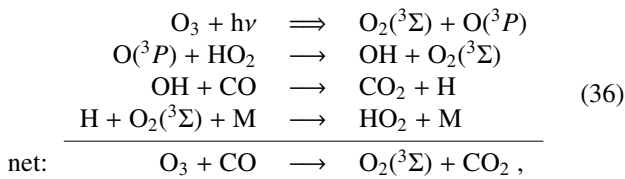
which includes the reaction



reconsidered by Krasnopolsky (1993), who recognized its importance in breaking the  $\text{O}_2$  bond to produce odd oxygen. Pathway (34) was already discussed by Stock et al. (2012b) but in the context of  $\text{CO}_2$  formation on Mars. This pathway is also relevant for the  $\text{CO}$  oxidation and  $\text{O}_3$  formation in Earth's troposphere (Brasseur et al., 1999) with M being  $\text{N}_2$  or  $\text{O}_2$  instead of  $\text{CO}_2$ .

### 3.2.2. Ozone consumption (lower region)

The dominant  $O_3$  removal process belongs to the pathway family



(see Section 2.2 for the definition of the “ $\Longrightarrow$ ”-symbol) the rate of which decreases with decreasing altitude (see Fig. 3). This

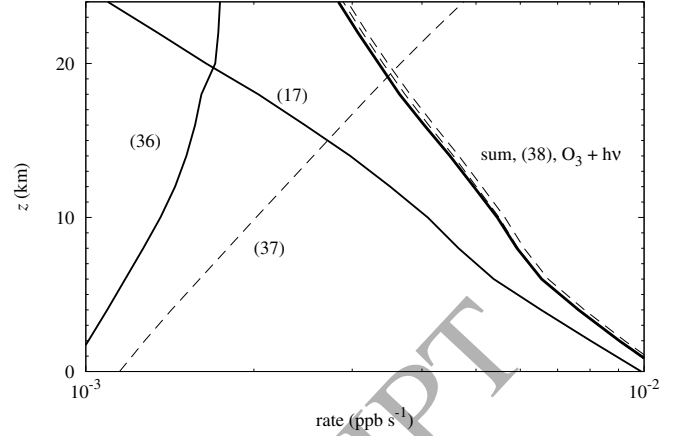
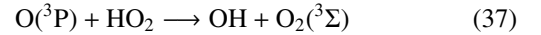
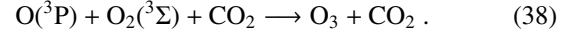


Figure 4: Rates  $\varphi_{ik}$  of the dominant  $O_3$  consumption pathway family (36) and the null pathway family (17) in the lower region (solid lines). Dashed lines refer to reactions (37), (38) and the photolysis  $\text{O}_3 + h\nu \longrightarrow \text{O}_2(^3\Sigma) + \text{O}(^3P)$ . The sum of the pathway family (36) and (17) is indicated by the bold solid line.

decrease is a result of increasing competition with the null pathway family (17) for  $\text{O}(^3P)$  produced by the  $\text{O}_3$  photolysis reaction (see Fig. 4). The rate of the  $\text{O}_3$  photolysis reaction is almost completely distributed to the pathway families (17) and (36). It is therefore sufficient to examine the ratio of the reactions



and



The ratio decreases with decreasing altitude (see Fig. 4), because of the increase in total number density and hence an increase of the rate of the three body reaction (38) and due to the decrease of the  $\text{HO}_2$  volume mixing ratio with decreasing altitude.

### 3.3. Chemical pathways in the upper region

Under global mean conditions, in the upper region,  $\mathcal{P}_{O_3}$  varies by more than one order of magnitude, whereas  $\hat{\Lambda}_{O_3}$  remains relatively constant, suggesting that the  $O_3$  layer is determined by the variation of the  $O_3$  production rate with atmospheric height (see Fig. 5). The major  $O_3$  producing/consuming pathways contributing to these rates are shown in Fig. 6 and Tab. 2. The rates are considerably larger than the rates of the pathways operating in the lower region (cf. Fig. 3). This provides additional evidence for two distinct chemical regimes in the  $O_3$  chemistry of Mars, indicating an especially active  $O_3$  chemistry in the upper region.

#### 3.3.1. Ozone production (upper region)

As seen in Fig. 5 the  $O_3$  volume mixing ratio profile is strongly affected by the production rate. Our results (Fig. 6) suggest that  $O_3$  production is almost exclusively dominated by the single termolecular recombination reaction (38). Since the  $\text{O}_2(^3\Sigma)$  and  $\text{CO}_2$  volume mixing ratios remain relatively constant with

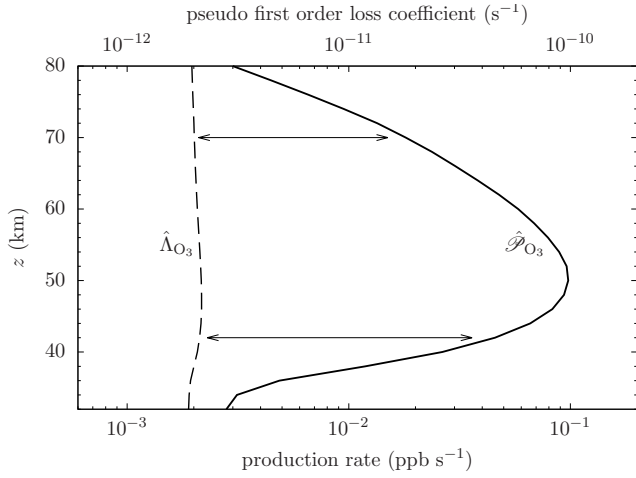


Figure 5: Ozone production rate (solid line) and pseudo first order  $O_3$  loss rate coefficient (dashed line) calculated according to Eq. (24) and Eq. (30). Since the  $x$ -axis is in logarithmic scale, the difference between the solid lines, indicated by the length of the horizontal arrows, describes the ratio  $\hat{\mathcal{P}}_{O_3} : \hat{\Lambda}_{O_3}$ , which is the volume mixing ratio of  $O_3$  according to Eq. (31).

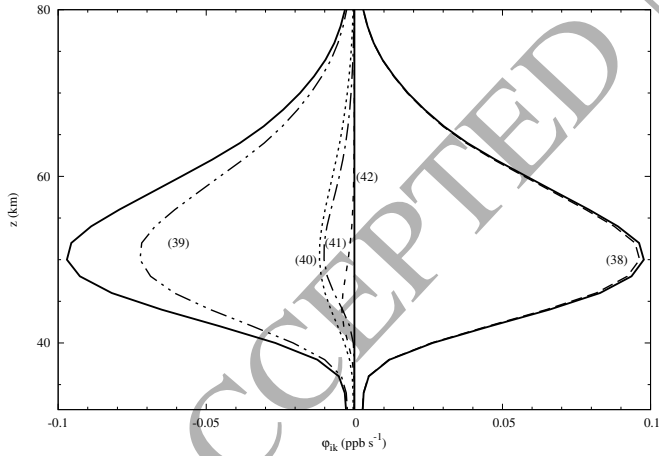


Figure 6: Rates  $\varphi_{ik}$  of  $O_3$  production/consumption pathways. Loss rates are indicated with a negative sign. The solid line on the right hand side indicates the production of  $O_3$  by all  $O_3$  formation pathways. The solid line on the left hand side indicates the consumption of  $O_3$  by all  $O_3$  consumption pathways. Bracketed numbers refer to pathways given in the text and Tab. 2.

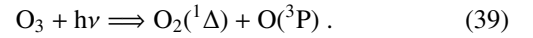
Table 2: Percentage contribution of the dominant  $O_3$  production and consumption pathways in the mid atmospheric  $O_3$  layer ( $z \approx 50$  km).

| production  |   |            |
|-------------|---|------------|
| (38)        | $O(^3P) + O_2(^3\Sigma) + CO_2 \longrightarrow O_3 + CO_2$                                      | <b>99%</b> |
| consumption |   |            |
| (39)        | $O_3 + h\nu \Longrightarrow O_2(^1\Delta) + O(^3P)$   | <b>75%</b> |
| (40)        | $O_3 + h\nu \longrightarrow O_2(^3\Sigma) + O(^3P)$   | <b>12%</b> |
| (41)        | $H + O_3 \longrightarrow OH + O_2(^3\Sigma)$<br>$O(^3P) + OH \longrightarrow O_2(^3\Sigma) + H$ |            |
| net:        | $O_3 + O(^3P) \longrightarrow 2 \cdot O_2(^3\Sigma)$  | <b>11%</b> |
| (42)        | $H + O_3 \longrightarrow OH + O_2(^3\Sigma)$<br>$OH + CO \longrightarrow CO_2 + H$              |            |
| net:        | $O_3 + CO \longrightarrow O_2(^3\Sigma) + CO_2$   | <b>2%</b>  |

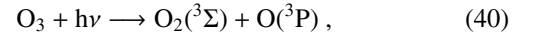
altitude (see Fig. 1(a)), the strong increase of the  $O(^3P)$  volume mixing ratio with increasing altitude leads to an increase in the  $O_3$  production rate and, hence, to an increase in the  $O_3$  volume mixing ratio, which peaks around  $z = 50$  km. The decrease of the  $O_3$  production rate with increasing altitude above  $z = 50$  km is due to the decrease of the total number density  $n_{tot}$  and thus the decrease in the rate of the termolecular reaction (38). The mechanism controlling the  $O(^3P)$  abundance in this region is of particular interest, since there  $O(^3P)$  is the dominant  $O_x$ -species (see Fig. 1(a)). Pathways producing/consuming  $O(^3P)$  and their effect on the  $O_3$  profile are discussed in Section 3.3.3.

### 3.3.2. Ozone consumption (upper region)

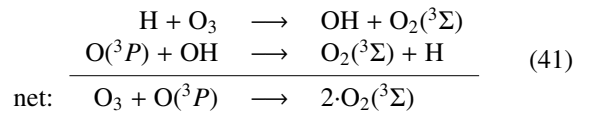
Figure 6 shows also the contributions of  $O_3$  consumption pathways in the upper region. In this part of the atmosphere  $O_3$  is mainly destroyed by photolysis and subsequent thermal deactivation of  $O(^1D)$



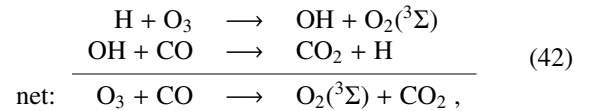
A less efficient alternative is the photolysis branch of  $O_3$



yielding the ground states of molecular  $O_2(^3\Sigma)$  and atomic oxygen  $O(^3P)$ . It is also possible that  $O_3$  is removed by reaction with H via the following two pathways



and



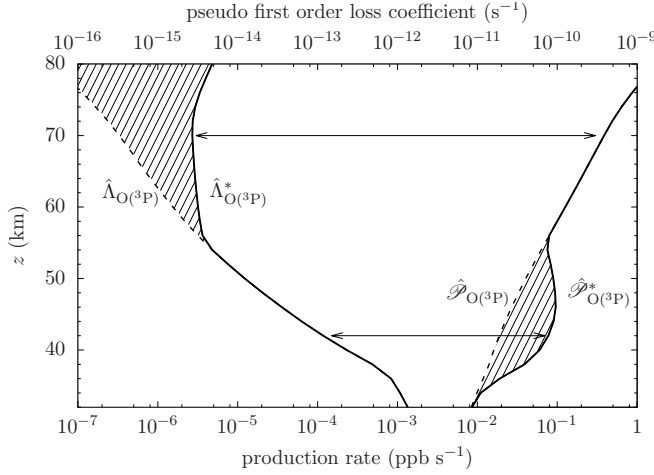


Figure 7: Pseudo first order  $O(^3P)$  loss rate coefficients  $\hat{\Lambda}_{O(^3P)}$  and  $\hat{\Lambda}_{O(^3P)}^*$  (left branch, upper axis) and  $O(^3P)$  production rates  $\hat{\mathcal{P}}_{O(^3P)}$  and  $\hat{\mathcal{P}}_{O(^3P)}^*$  (right branch, lower axis). Solid lines refer to calculations where vertical transport is included as pseudo reactions according to Eq. (43) and (44), whereas dashed lines refer to calculations where vertical transport of  $O(^3P)$  is not included. Hatched areas illustrate the effect of vertical transport. Since the x-axis is in logarithmic scale, the difference between the solid lines, indicated by the length of the horizontal arrows, describes the ratio  $\hat{\mathcal{P}}_{O(^3P)} : \hat{\Lambda}_{O(^3P)}$ , which is the volume mixing ratio of  $O(^3P)$  according to Eq. (31).

which however are less efficient as seen in Fig. 6. For real Mars conditions, the hydropause depends on the season and can rise to higher altitudes during the summer, leading to an increase in the  $HO_x$  volume mixing ratio, which in turn, results in the disappearance of the  $O_3$  layer (Clancy et al., 1996; Lefevre et al., 2004). These observations are consistent with our results. Moreover, the presence of ice clouds can reduce the  $HO_x$  volume mixing ratio (see e.g. Anbar et al., 1993; Lefevre et al., 2008), which decreases the rates of pathways (41) and (42) – thus increasing the  $O_3$  volume mixing ratio.

### 3.3.3. Atomic oxygen production and consumption (upper region)

In contrast to the lower region, in the upper region  $O(^3P)$  is more abundant than  $O_3$  (see Fig. 1(a)). In order to understand why  $O(^3P)$  is so abundant in this part of the atmosphere, we use the *PAP* algorithm to also study the  $O(^3P)$  pathways. Figure 7 shows the production/consumption of  $O(^3P)$  by chemical pathways with and without transport. We denote the  $O(^3P)$  production rate by  $\hat{\mathcal{P}}_{O(^3P)}$  if vertical mixing is included as a pseudo reaction (see Section 2.2) and the pseudo first order  $O(^3P)$  loss rate coefficient  $\hat{\Lambda}_{O(^3P)}^*$  accordingly. These quantities are related to the chemical  $O(^3P)$  production rate and the pseudo first order chemical  $O(^3P)$  loss rate coefficient via

$$\hat{\mathcal{P}}_{O(^3P)}^* = \hat{\mathcal{P}}_{O(^3P)} + r_{O(^3P)}^{\text{gain}} \quad (43)$$

$$\hat{\Lambda}_{O(^3P)}^* = \hat{\Lambda}_{O(^3P)} + \frac{r_{O(^3P)}^{\text{loss}}}{n_{O(^3P)}} \quad (44)$$

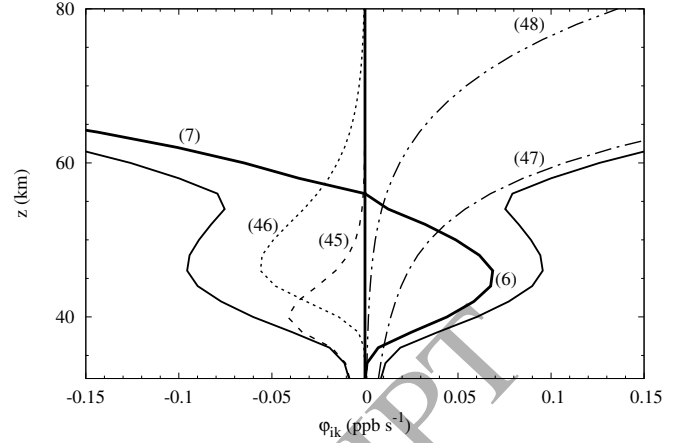
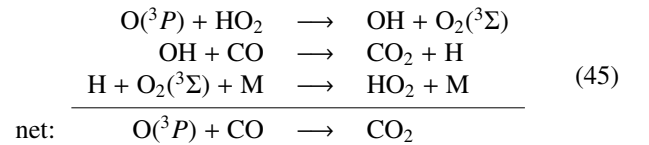


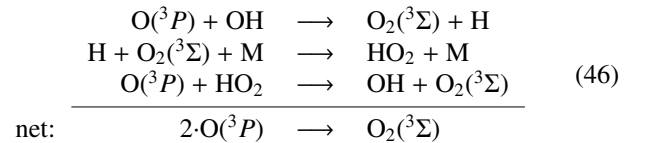
Figure 8: Rates  $\phi_{ik}$  of  $O(^3P)$  production/consumption pathways. Loss rates are indicated with a negative sign. The solid line on the right hand side indicates the production of  $O(^3P)$  by all  $O(^3P)$  formation pathways. The solid line on the left hand side indicates the consumption of  $O(^3P)$  by all  $O(^3P)$  consumption pathways. The thick solid lines on the refer to the transport pathways (6) and (7). Pathways are summarized in Tab. 3.

where  $r_{O(^3P)}^{\text{gain}}$  and  $r_{O(^3P)}^{\text{loss}}$  are defined by Eq. (8) and Eq. (9). As it can be seen in Fig. 7, there is a net transport of  $O(^3P)$  from upper atmospheric layers ( $z > 56$  km) to lower altitudes ( $32 \text{ km} \lesssim z \lesssim 56 \text{ km}$ ).

The  $O(^3P)$  production rate  $\hat{\mathcal{P}}_{O(^3P)}^*$  increases by about one order of magnitude with increasing altitude between  $z = 32$  km and  $z = 56$  km, whereas the pseudo first order  $O(^3P)$  loss rate coefficient  $\hat{\Lambda}_{O(^3P)}^*$  decreases by more than two orders of magnitude. This results in an increase of the  $O(^3P)$  volume mixing ratio with increasing altitude, which is predominantly determined by the  $O(^3P)$  consumption. Figure 8 shows that the pathways



and



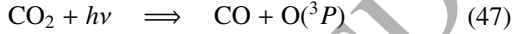
are the most important  $O(^3P)$  consumption pathways between  $z = 32$  km and  $z = 60$  km. Pathway (45) was discussed in the context of the  $CO_2$  stability problem by e.g. McElroy and Donahue (1972), Nair et al. (1994) and Stock et al. (2012a). The rates of both pathways (45) and (46) depend on the abundance of  $HO_x$ . The change in the slope of  $\hat{\Lambda}_{O(^3P)}$  at  $z \approx 36$  km

Table 3: Percentage contribution of the dominant  $O(^3P)$  production and consumption pathways in the mid atmospheric  $O_3$  layer ( $z \approx 50$  km).

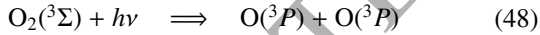
| production  |   |            |
|-------------|---|------------|
| (6)         | $O(^3P)[\text{adjacent layer(s)}] \rightarrow O(^3P)$   | <b>55%</b> |
| (47)        | $CO_2 + h\nu \Rightarrow CO + O(^3P)$   | <b>39%</b> |
| (48)        | $O_2(^3\Sigma) + h\nu \Rightarrow O(^3P) + O(^3P)$  | <b>6%</b>  |
| consumption |   |            |
| (45)        | $O(^3P) + HO_2 \rightarrow OH + O_2(^3\Sigma)$<br>$OH + CO \rightarrow CO_2 + H$<br>$H + O_2(^3\Sigma) + M \rightarrow HO_2 + M$              |            |
| net:        | $O(^3P) + CO \rightarrow CO_2$  | <b>55%</b> |
| (46)        | $O(^3P) + OH \rightarrow O_2(^3\Sigma) + H$<br>$H + O_2(^3\Sigma) + M \rightarrow HO_2 + M$<br>$O(^3P) + HO_2 \rightarrow OH + O_2(^3\Sigma)$ |            |
| net:        | $2 \cdot O(^3P) \rightarrow O_2(^3\Sigma)$  | <b>23%</b> |

(Fig. 7) correlates with the abrupt decrease in  $HO_2$  volume mixing ratio (Fig. 1(a)), suggesting that a “dry” atmosphere (i.e. “lack” of OH and especially  $HO_2$ ) leads to an increase in the  $O(^3P)$  volume mixing ratio. Figure 8 also suggests that above  $z \approx 58$  km,  $O(^3P)$  removal via transport dominates. The corresponding pathway includes only the pseudo reaction (7).

Atomic oxygen  $O(^3P)$  is produced directly by  $CO_2$  photolysis



and  $O_2$  photolysis



$O(^3P)$  is then transported downwards to the  $O_3$  layer of the upper region. The corresponding pathway includes only the pseudo reaction (6). In order to illustrate the effect of vertical transport of  $O(^3P)$  on the  $O_3$  profile, we calculate first the concentration profiles of  $O(^3P)$  in the absence of  $O(^3P)$  transport, i.e.

$$n_{O(^3P)}^o = \frac{\hat{P}_{O(^3P)}}{\hat{\Lambda}_{O(^3P)}}. \quad (49)$$

Note that  $\hat{P}_{O(^3P)}$  and  $\hat{\Lambda}_{O(^3P)}$  do not include the transport pseudo reactions (6) and (7). Figure 9(a) shows that vertical transport leads to an increase in  $O(^3P)$  volume mixing ratio below  $z = 56$  km and a decrease above  $z = 56$  km consistent with Fig. 7. This indicates that  $O(^3P)$  is effectively transported downwards. To estimate the effect of  $O(^3P)$  transport on the  $O_3$  profile, we use  $n_{O(^3P)}^o$  from Eq. (49), in order to derive a hypothetical  $O_3$  profile that would be formed in the absence of  $O(^3P)$  transport. Figure 6 suggests that we can approximate  $\hat{P}_{O_3}$  by  $r_{38}$ . We use the modified concentration  $n_{O(^3P)}^o$ , when computing the rate of reaction (38), henceforth called  $r_{38}^o$ , i.e. we exclude

the effect of  $O(^3P)$  transport without modifying the transport of other chemical species.  $\hat{\Lambda}_{O_3}$  depends on  $O(^3P)$  transport via pathway (41). Since, however, the rate of pathway (41) is considerably smaller than the rates of pathways (39) and (40),  $O(^3P)$  transport can be neglected in the calculation of  $\hat{\Lambda}_{O_3}$ . Nonetheless,  $O(^3P)$  transport can affect the OH-abundance via reaction (37), which in turn may influence the rates of the  $O_3$  consumption pathways (41) and (42). This effect is expected to be relatively small in comparison to the direct influence of  $O(^3P)$  transport on  $\hat{P}_{O_3}$  (see Fig. 6.). The hypothetical  $O_3$  profile – without  $O(^3P)$  transport – can then be calculated via

$$n_{O_3}^o \approx \frac{r_{38}^o}{\hat{\Lambda}_{O_3}}. \quad (50)$$

Figure 9(b) suggests that  $O(^3P)$  transport has two effects on the vertical  $O_3$  profile. Firstly, we find a larger  $O_3$  volume mixing ratio below  $z = 56$  km and a smaller  $O_3$  volume mixing ratio above  $z = 56$  km. Secondly, vertical transport of  $O(^3P)$  is essential for the formation of the local  $O_3$  maximum in the investigated altitude range. Since vertical transport of  $O(^3P)$  depends on the eddy diffusion profile, we expect, in accordance with McElroy and Donahue (1972) and Parkinson and Hunten (1972), the  $O_3$  profile to be sensitive to the eddy diffusion profile.

#### 3.4. Effect of the temperature profile on the $O_3$ layer

Reaction rate coefficients and the saturation pressure of  $H_2O$  are functions of temperature and inevitably affect the reaction rates in the chemical network. Hence, the  $HO_x$  abundance, and consequently, the  $O_3$  volume mixing ratio profile depend implicitly on temperature. Therefore, it might be theoretically possible that the characteristic  $O_3$  profile on Mars is mainly a consequence of a specific atmospheric temperature profile.

To investigate this effect, we calculate the volume mixing ratios using an *idealized* temperature profile, which is constant ( $T_{av} = 176.5$  K) up to  $z = 136$  km and then follows our standard temperature profile adopted from Nair et al. (1994). The value  $T_{av}$  is the arithmetic mean of the surface temperature and the minimum temperature in the standard case. The lower altitude atmospheric temperature causes a larger amount of  $H_2O$  to condense, resulting in less  $HO_x$ . Hence the  $O_3$  abundance increases by about two orders of magnitude (see Fig. 10(a)). In the upper region the modified temperature profile has no significant effect on the  $H_2O$  and  $O_3$  abundances and the  $O_3$  profile, i.e. the mid-atmospheric  $O_3$  layer still exists (see Figs. 10(a) and 10(b)). This means that the change in temperature with altitude is not responsible for the formation of the  $O_3$  layer.

## 4. Conclusions

We provide the first quantitative pathway analysis of the Martian atmospheric  $O_3$  profile by applying the *Pathway Analysis Program (PAP)* for the first time to the output of the updated JPL/Caltech KINETICS model in order to gain a better understanding of the relevant chemical and transport processes and therefore also a better understanding of observable features.

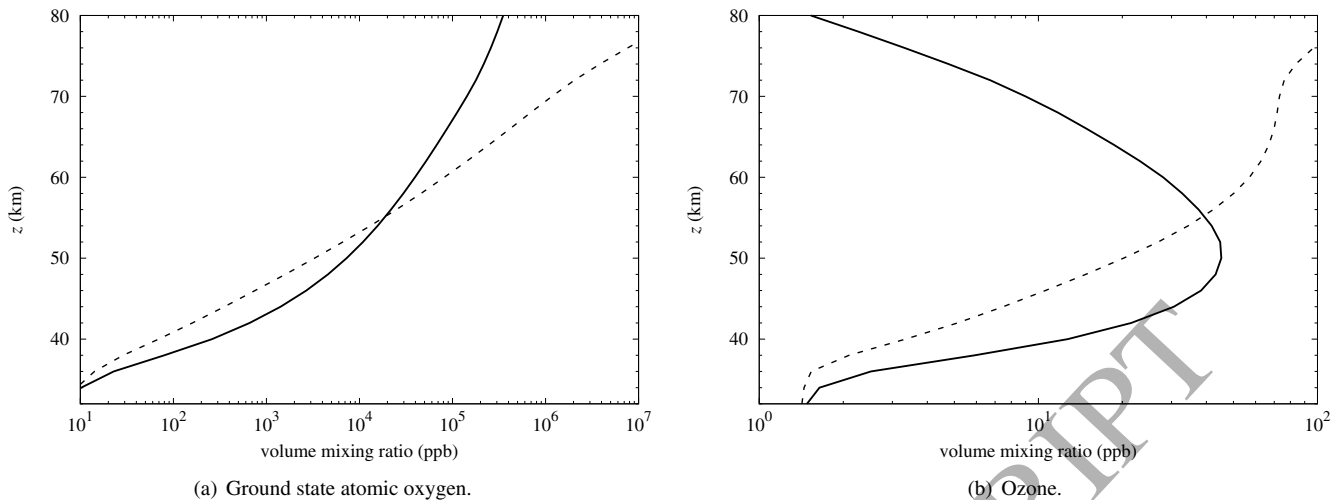


Figure 9: Volume mixing ratios of  $O(^3P)$  and  $O_3$ . Solid lines indicate the profiles calculated by the Caltech/JPL KINETICS model. Dashed lines refer to the volume mixing ratio profiles  $n_i^o/n_{tot}$  estimated in the absence of  $O(^3P)$  transport.

From inspection of the concentrations of  $O(^3P)$  and  $O_3$  and as a result of our analysis, the Martian atmosphere can be divided into two chemically distinct regions. In the lower region, the dominant  $O_x$  species is  $O_3$  and in the upper region the dominant  $O_x$  species is  $O(^3P)$ . These regions differ significantly in the manner in which processes control the  $O_3$  abundance.

The pathway analysis confirms, that in the lower region,  $O_3$  is formed by a Chapman-like mechanism, involving  $CO_2$  photolysis (instead of  $O_2$  photolysis as on Earth), which is consistent with earlier findings by e.g. McElroy and Donahue (1972). On Mars  $O_3$  consumption proceeds via pathways involving  $HO_x$ . The decrease of the total  $O_3$  loss rate coefficient with decreasing altitude leads to the formation of the ground layer  $O_3$  maximum. Most of the  $O_3$ , destroyed via photolysis, is recycled back.

In the upper region,  $O(^3P)$  is the dominant  $O_x$  species. Therefore, we further analyzed  $O(^3P)$  production and consumption between  $z \approx 32$  km and  $z \approx 80$  km. The additional *PAP* analysis shows in accordance with Parkinson and Hunten (1972) and Krasnopolsky (1993) that the main reason for the high abundance of  $O(^3P)$  is the small concentration of  $OH$  and  $HO_2$  above  $z \approx 35$  km altitude. In the upper region  $O_3$  is produced by one reaction, namely  $O(^3P) + O_2(^3\Sigma) + CO_2 \rightarrow O_3 + CO_2$ , which critically depends on the downward transport of  $O(^3P)$  from upper atmospheric layers ( $z > 56$  km) into the Martian  $O_3$  layer. There,  $O_3$  is mainly removed by photolysis and to some part by reaction with  $H$ , which is subsequently recycled. Although clearly,  $O_3$  consumption pathways are important to regulate the absolute abundance of  $O_3$ , the shape of the  $O_3$  profile is mainly determined by the  $O_3$  production mechanism. The increase of the  $O_3$  volume mixing ratio below  $z = 50$  km is due to the strong increase of  $O(^3P)$  with increasing altitude, which in turn can be explained by the decreasing concentration of  $OH$  and  $HO_2$ . The decrease of the  $O_3$  volume mixing ratio with increasing altitude above  $z = 50$  km is a result of the decreasing rate of the ter-

molecular reaction  $O(^3P) + O_2(^3\Sigma) + CO_2 \rightarrow O_3 + CO_2$ .

Recent observations (Clancy et al., 2013; Rezac et al., 2015; Villanueva et al., 2013) demonstrate that many of the species relevant for the  $O_3$  chemistry ( $OH$ ,  $O$ ,  $HO_2$ ) are now detectable. To improve our understanding of the Martian atmospheric  $O_3$  profile, simultaneous measurements of these species in combination with  $H_2O$  and  $O_3$  would be desirable.

## Acknowledgment

This research has been partly supported by the Helmholtz Association through the research alliance “Planetary Evolution and Life”. This work was partially funded by grant AyA 2012–32237 awarded by the Spanish Ministerio de Economía y Competitividad. The authors would like to thank Run-Lie Shia and Dickens Saint-Hilaire for their contributions to the discussion.

## References

- Anbar, A.D., Leu, M.-T., Nair, H.A., Yung, Y.L., 1993. Adsorption of  $HO_x$  on aerosol surfaces: Implications for the atmosphere of Mars. *J. Geophys. Res.*, 98, 10933-10940.
- Anderson, E., Leovy, C., 1978. Mariner 9 television limb observations of dust and ice hazes on Mars. *J. Atmos. Sci.*, 35, 723-734.
- Atreya, S.K., Gu, Z.G., 1994. Stability of the Martian atmosphere: Is heterogeneous catalysis essential? *J. Geophys. Res.*, 99, 13133-13145.
- Barker, E.S., 1976. Martian atmospheric water vapor observations – 1972-74 apparition. *Icarus*, 28, 247-268.
- Barth, C.A., Hord, C.W., 1971. Mariner ultraviolet spectrometer: Topography and polar cap. *Science*, 173, 197-201.
- Barth, C.A., Hord, C.W., Stewart, A.I., Lane, A.L., Disk, M.L., Anderson, G.P., 1973. Mariner 9 ultraviolet spectrometer experiment: Seasonal variations of ozone on Mars. *Science*, 179, 795-796.
- Bates, D.R., Nicolet, M., 1950. The photochemistry of atmospheric water vapour. *J. Geophys. Res.*, 55, 301-327.
- Bertaux, J.-L., et al., 2000. The study of the Martian atmosphere from top to bottom with SPICAM light on Mars Express. *Planet. Space Sci.*, 48, 1303-1320.

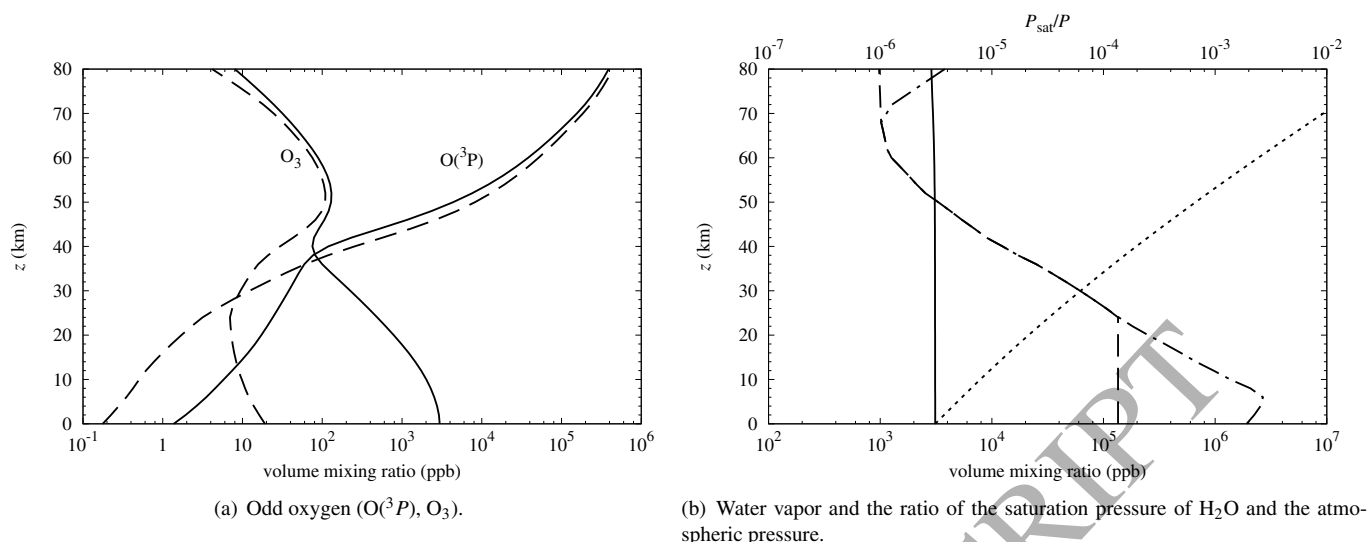


Figure 10: Volume mixing ratios of selected species in the Martian atmosphere calculated by the Caltech/JPL KINETICS model. Solid lines refer to the scenario with the modified temperature profile (see text), dashed lines refer to the “standard” scenario. Dotted line (right hand panel) refer to the ratio  $P_{sat}/P$  (modified temperature profile), dot-dashed line refer to the ratio  $P_{sat}/P$  (“standard” scenario).

- Bertaux, J.-L., et al., 2006. SPICAM on Mars Express: Observing modes and overview of UV spectrometer data and scientific results. *J. Geophys. Res.*, 111, E10S90.
- Blamont, J.E., Chassefière, E., 1993. First detection of ozone in the middle atmosphere of Mars from solar occultation measurements. *Icarus*, 104, 324-336.
- Boxe, C.S., et al., 2014. New insights into martian atmospheric chemistry. *Icarus*, 242, 97-104.
- Brasseur, G.P., Orlando, J., Tyndall, G., 1999. *Atmospheric Chemistry and Global Change*. Oxford University Press, New York.
- Chapman, S., 1930. A theory of upper-atmosphere ozone. *Memoirs of the Royal Meteorological Society*, 3, 103-125.
- Chassefière, E., Blamont, J.E., Krasnopolsky, V.A., Korabiev, O.I., Atreya, S.K., West R.A., 1992. Vertical structure and size distributions of martian aerosols from solar occultation measurements. *Icarus*, 97, 46-69.
- Clancy, R.T., Nair, H., 1996. Annual (perihelion-aphelion) cycles in the photochemical behavior of the global Mars atmosphere. *J. Geophys. Res.*, 101, 12785-12790.
- Clancy, R.T. et al., 2013. First detection of Mars atmospheric hydroxyl: CRISM Near-IR measurement versus LMD GCM simulation of OH Meinel band emission in the Mars polar winter atmosphere. *Icarus*, 226, 272-281.
- Clancy, R.T., Wolff, M.J., Lefèvre, F., Cantor, B.A., Malin, M.C., Smith, M.D., 2016. Daily global mapping of Mars ozone column abundances with MARCI UV band imaging. *Icarus*, 266, 112-133.
- Crutzen, P.J., 1970. The influence of nitrogen oxides on the atmospheric ozone content. *Quart. J. R. Met. Soc.*, 96, 320-325.
- Espenak, F., Mumma, M.J., Kostiuik, T., Zipoy, D., 1991. Ground-based infrared measurements of the global distribution of ozone in the atmosphere of Mars. *Icarus*, 92, 252-262.
- Fast et al., 2006. Ozone abundance on Mars from infrared heterodyne spectra I. Acquisition, retrieval, and anticorrelation with water vapor. *Icarus*, 181, 491-431.
- Fast et al., 2006. Ozone abundance on Mars from infrared heterodyne spectra II. Validating photochemical models. *Icarus*, 183, 396-402.
- Grenfell, J.L., Lehmann, R., Mieth, P., Langematz, U., Steil, B., 2006. Chemical reaction pathways affecting stratospheric and mesospheric ozone. *J. Geophys. Res.*, 111, D17311.
- Grenfell, J.L., Gebauer, S., Godolt, M., Palczynski, K., Rauer, H., Stock, J., von Paris, P., Lehmann, R., Selsis, F., 2013. Potential biosignatures in Super-Earth atmospheres II. Photochemical responses. *Astrobiology*, 13, 415-438.
- Houben, H., Haberle, R.M., Young, R.E., Zent, A.P., 1997. Modeling the Martian seasonal water cycle. *J. Geophys. Res.*, 102, 9069-9084.
- Jacobson, M.Z., 2005. *Fundamentals of Atmospheric Modeling*. Cambridge University Press, New York.
- Jakosky, B.M., 1985. The seasonal cycle of water on Mars, *Space Science Reviews*, 41, 131-200.
- Jakosky, B.M., Farmer, C.B., 1982. The seasonal and global behavior of water vapor in the Mars atmosphere – Complete global results of the Viking atmospheric water detector experiment. *J. Geophys. Res.*, 87, 2999-3019.
- Korabiev, O.I., Krasnopolsky, V.A., Rodin, A.V., Chassefière, E., 1993. Vertical structure of martian dust measured by solar infrared occultations from the *Phobos* spacecraft. *Icarus*, 102, 76-87.
- Krasnopolsky, V.A., 1993. Photochemistry of the martian atmosphere (mean conditions). *Icarus*, 101, 313-332.
- Krasnopolsky, V.A., 2003. Mapping of Mars  $O_2$  1.27- $\mu$ m dayglow at four seasonal points. *Icarus*, 165, 315-325.
- Krasnopolsky, V.A., Bjoraker, G.L., 2000. Mapping of Mars  $O_2(^1\Delta)$  dayglow. *J. Geophys. Res.*, 105(E8), 20179-20188.
- Krasnopolsky, V.A., Krysko, A.A., Rogachev, V.N., 1975. Measurement of ozone in a planetary atmosphere by space probe Mars-5. *Kosmicheskie Issledovaniia*, 13, 37-41 (translation: *Cosmic Research*, 13, 31-34).
- Krasnopolsky, V.A., Parshev, V.A., 1979. Ozone and photochemistry of the Martian lower atmosphere. *Planet. Space Sci.*, 27, 113-120.
- Lane, A.L., Barth, C.A., Hord, C.W., Stewart, A.I., 1973. Mariner 9 ultraviolet spectrometer: Observations of ozone on Mars. *Icarus*, 18, 102-108.
- Lebonnois, S. et al., 2006. Vertical distribution of ozone on Mars as measured by SPICAM/Mars Express using stellar occultations. *J. Geophys. Res.*, 111, E09S06.
- Lehmann, R., 2004. An algorithm for the determination of all significant pathways in chemical reaction systems. *Journal of Atmospheric Chemistry*, 47, 45-78.
- Lefèvre, F., Lebonnois, S., Montmessin, F., Forget, F., 2004. Three-dimensional modeling of ozone on Mars. *J. Geophys. Res.*, 109, E07004.
- Lefèvre, et al., 2008. Heterogeneous chemistry in the atmosphere of Mars. *Nature*, 454, 971-975.
- Matsumi, et al., 2002. Quantum yields for production of  $O(^1D)$  in the ultraviolet photolysis of ozone: Recommendation based on evaluation of laboratory data. *J. Geophys. Res.*, 107(D3), 2156-2202.
- McConnell, J.C., McElroy, M.B., 1973. Odd nitrogen in the atmosphere. *J. Atmos. Sci.*, 30, 1465-1480.
- McElroy, M.B., Donahue, T.M., 1972. Stability of the Martian atmosphere. *Science*, 177, 986-988.
- Montmessin, F., Forget, F., Rannou, P., Cabane, M., Haberle, R.M., 2004. Origin and role of water ice clouds in the Martian water cycle inferred from a

- general circulation model. *J. Geophys. Res.*, 109, E10004.
- Nair, H., Allen, M., Anbar, A.D., Yung, Y.L., 1994. A photochemical model of the martian atmosphere. *Icarus*, 111, 124-150.
- Novak, R.E., Mumma, M.J., DiSanti, M.A., Dello Russo, N., 2002. Mapping of ozone and water in the atmosphere of Mars near the 1997 aphelion. *Icarus*, 158, 14-23.
- Noxon, J.F., Traub, W.A., Carleton, N.P., Connes, P., 1976. Detection of O<sub>2</sub> dayglow emission from Mars and the Martian ozone abundance. *Astrophys. J.*, 207, 1025-1035.
- Parkinson, T.M., Hunten, D.M., 1972. Spectroscopy and aeronomy of O<sub>2</sub> on Mars. *J. Atmos. Sci.*, 29, 1380-1390.
- Perrier, s. et al., 2006. Global distribution of total ozone on Mars from SPICAM/MEX UV measurements. *J. Geophys. Res.*, 111, E09S06.
- Rezac, L., et al., 2015. First detection of the 63  $\mu$ m atomic oxygen line in the thermosphere of Mars with GREAT/SOFIA. *Astron. Astrophys.*, 580, L10.
- Richardson, M.I., Wilson, R.J., 2002. Investigation of the nature and stability of the Martian seasonal water cycle with a general circulation model. *J. Geophys. Res. (Planets)*, 107, E55031.
- Rosenqvist, J., Chassefière, E., 1995. A reexamination of the relationship between eddy mixing and O<sub>2</sub> in the Martian middle atmosphere. *J. Geophys. Res.*, 100, 5541-5551.
- Sander, S.P., et al., 2011. Chemical Kinetics and Photochemical Data for use in Atmospheric Studies. Evaluation number 17, JPL Publ. 10-6.
- Schuster, R., Schuster, S., 1993. Refined algorithm and computer program for calculating all nonnegative fluxes admissible in steady states of biochemical reaction systems with or without some flux rates fixed. *Computer Applications in Biosciences*, 9, 79-85.
- Smith, M.D., 2004. Interannual variability in TES atmospheric observations of Mars during 1999-2003. *Icarus*, 167, 148-165.
- Stock, J.W., et al., 2012. Chemical pathway analysis of the Martian atmosphere: CO<sub>2</sub>-formation pathways. *Icarus*, 219, 13-14.
- Stock, J.W., Grenfell, J.L., Lehmann, R., Patzer, A.B.C., Rauer, H., 2012. Chemical pathway analysis of the lower Martian atmosphere: The CO<sub>2</sub> stability problem. *Planet. Space Sci.* 68, 18-24.
- Toon, O.B., Pollack, J.B., Sagan, C., 1977. Physical properties of the particles composing the martian dust storm of 1971-1972. *Icarus*, 30, 663-696.
- Traub, W.A., Carleton, N.P., Connes, P., Noxon, J.F., 1979. The latitude variation of O<sub>2</sub> dayglow and O<sub>3</sub> abundance on Mars. *Astrophys. J.*, 229, 846-854.
- Verronen, P.T., Lehmann, R., 2013. Analysis and parameterization of ionic reactions affecting middleatmospheric HO<sub>x</sub> and NO<sub>x</sub> during solar proton events. *Annales Geophysicae*, 31, 909-956.
- Verronen, P.T., Lehmann, R., 2015. Enhancement of odd-nitrogen modifies mesospheric ozone chemistry during polar winter. *Geophys. Res. Lett.*, 42, 10445-10452, 2015.
- Verronen P.T., Santee M.L., Manney G.L., Lehmann R., Salmi S.-M., Seppälä, A., 2011. Nitric acid enhancements in the mesosphere during January 2005 and December 2006 solar proton events. *J. Geophys. Res.*, 116, D17301.
- Villanueva, G.L., et al., 2013. A sensitive search for organics (CH<sub>4</sub>, CH<sub>3</sub>OH, H<sub>2</sub>CO, C<sub>2</sub>H<sub>6</sub>, C<sub>2</sub>H<sub>2</sub>, C<sub>2</sub>H<sub>4</sub>), hydroperoxyl (HO<sub>2</sub>), nitrogen compounds (N<sub>2</sub>O, NH<sub>3</sub>, HCN) and chlorine species (HCl, CH<sub>3</sub>Cl) on Mars using ground-based high-resolution infrared spectroscopy. *Icarus*, 223, 11-27.
- Wehrbein, W.M., Hord, C.W., Barth, C.A., 1979. Mariner 9 ultraviolet spectrometer experiment: Vertical distribution of ozone on Mars. *Icarus*, 38, 188-199.
- Yung, Y.L., DeMore, W.B., 1999. Photochemistry of Planetary Atmospheres. Oxford University Press, New York.